Investigation of (mis-)orientation in zincblende GaN grown on micro-patterned Si(001) using electron backscatter diffraction ⊘

Dale M. Waters ⓘ ; Bethany Thompson ⓘ ; Gergely Ferenczi ⓘ ; Ben Hourahine ⓘ ; Grzegorz Cios ⓘ ; Aimo Winkelmann ⓘ ; Christoph J. M. Stark ⓘ ; Christian Wetzel ⓘ ; Carol Trager-Cowan ⓘ ; Jochen Bruckbauer ✉ ⓘ

Check for updates

⬚ CHORUS

View Online   Export Citation

Investigation of (mis-)orientation in zincblende GaN grown on micro-patterned Si(001) using electron backscatter diffraction

Dale M. Waters,[1] (ID) Bethany Thompson,[1] (ID) Gergely Ferenczi,[1] (ID) Ben Hourahine,[1,2] (ID) Grzegorz Cios,[3] (ID)
Aimo Winkelmann,[1,3] (ID) Christoph J. M. Stark,[4] (ID) Christian Wetzel,[4] (ID) Carol Trager-Cowan,[1] (ID)
and Jochen Bruckbauer[1,a)] (ID)

AFFILIATIONS

[1]Advanced Materials Diffraction Lab, Department of Physics, SUPA, University of Strathclyde, Glasgow G4 0NG, Scotland,
United Kingdom
[2]Computational Nonlinear and Quantum Optics Group, Department of Physics, SUPA, University of Strathclyde, Glasgow G4 0NG,
Scotland, United Kingdom
[3]Academic Centre for Materials and Nanotechnology, AGH University of Krakow, Kraków 30-059, Poland
[4]Department of Materials Science and Engineering and Department of Physics, Applied Physics and Astronomy,
Rensselaer Polytechnic Institute, Troy, New York 12180, USA

[a)]**Author to whom correspondence should be addressed:** jochen.bruckbauer@strath.ac.uk

ABSTRACT

We present the application of electron backscatter diffraction (EBSD) as a technique for characterizing wurtzite (wz) and zincblende (zb) polytypes of GaN grown upon micropatterned Si (001) substrates. The Si substrate is etched to create parallel V-shaped grooves with opposing {111} facets before the deposition of GaN. EBSD revealed that wz-GaN growth fronts initially form on the {111} Si facets before undergoing a transition from a wurtzite to zincblende structure as the two growth fronts meet. Orientation analysis of the GaN structures revealed that the wz-GaN growth fronts had different growth orientations but shared the same crystallographic relationship with the zb-GaN such that $\perp\{30\bar{3}8\}_{wz} \parallel \langle 110 \rangle_{zb}$, $\langle 11\bar{2}0 \rangle_{wz} \parallel \langle 110 \rangle_{zb}$, and $\perp\{30\bar{3}4\}_{wz} \parallel \langle 001 \rangle_{zb}$. Furthermore, the crystallographic relationship, $\{0001\}_{wz-GaN} \parallel \{111\}_{zb-GaN} \parallel \{111\}_{Si}$, and alignment of the wz- and zb-GaN with respect to the Si substrate was investigated. The two wz-GaN $\langle 0001 \rangle$ growth directions were expected to coalesce at an angle of 109.5°; however, measurements revealed an angle of 108°. The resultant misalignment of 1.5° induces misorientation in the zb-GaN crystal lattice. While the degree of misorientation within the zb-GaN lattice is low, $< 1°$, the zb-GaN lattice is deformed and bends toward the wz-GaN interfaces about the specimen direction parallel to the length of the V-groove. Further EBSD measurements over larger areas of the sample revealed that these results were consistent across the sample. However, it was also revealed that additional factors induce changes in the orientation of the zb-GaN lattice, which may relate to the initial growth conditions of the zb-GaN.

I. INTRODUCTION

White light-emitting diodes (LEDs) are valued in lighting applications for their advantages of small size, low energy consumption, high efficacy, and increased device longevity relative to conventional light sources. The widespread implementation of white LEDs is identified as a "high impact opportunity" by the United Nations Environment Programme and would reduce the global electricity demand for lighting by 30%–40%.[1] Prevalent white LED designs utilize blue InGaN/GaN LED chips coated in a phosphor to down convert the blue light to longer wavelengths. However, this process results in a loss of excitation energy, i.e., Stokes' loss, of the order of 25%.[2] In order to increase the potential

efficiency of white LEDs, it is necessary to circumvent the need for a phosphor. To achieve this, direct red, green, and blue (RGB) LEDs are required. However, to date, such devices have yet to produce white light with efficacies comparable to their phosphor-based counterparts.[3] The origin of this deficiency in direct white RGB LEDs is attributed to a drop in the external quantum efficiency (EQE) for LEDs operating in the yellow to green spectral region, referred to as the " green gap."[4] Devices based on green-emitting InGaN/GaN multiple quantum wells exhibit peak EQE of $\approx 56\%$,[5,6] whereas blue LEDs have EQEs exceeding 80%.[7] Furthermore, efficient green LEDs are also required for display applications using individual red, green, and blue LEDs for high-resolution displays with accurate color rendering where precise color mixing is important.[8,9]

For InGaN/GaN heterostructures, the green gap is usually attributed to the deterioration of material quality and reduction in the radiative recombination rate with increasing InN fraction in the active region.[4,9,10] GaN, and its alloys, are typically grown as the thermodynamically stable hexagonal, wurtzite crystal structure with a c-plane, or (0001), orientation. Wurtzite GaN (wz-GaN) is inherently polar along the c-axis, or [0001] direction, of its unit cell, making it prone to both spontaneous and piezoelectric polarization fields.[11] For (0001) oriented heterostructures, discontinuity in polarization at the heterojunctions causes sheets of opposite charge to build up at either interface, inducing large internal electric fields parallel to the c-axis. The electric field reduces the overlap of electron–hole wave functions in the active region and decreases the efficiency of radiative recombination, this is referred to as the quantum-confined Stark effect (QCSE).[12–14] To achieve deep green emission, high InN fraction is required in the active region of c-plane devices. However, because InGaN has a larger lattice parameter than GaN, increasing the InN fraction strengthens the effects of piezoelectric polarization through strain. While this is partially mitigated in c-plane material by reducing the thickness of the quantum wells,[15] relatively prolonged excitonic lifetimes and reduced quantum efficiencies are observed for green-emitting devices.[16]

As polarization fields are normal to the c-plane, growth along perpendicular orientations (i.e., the a-plane and m-plane) is a potential alternative to avoid polarization effects.[17] It has been demonstrated that the QCSE is absent from non-polar wz-GaN, which exhibits significantly shorter radiative lifetimes and stronger overlap between electron–hole wave functions relative to c-plane oriented material.[18–20] However, the EQE of non-polar orientations of wz-GaN LEDs have yet to surpass their c-plane counterparts.[21] A possible explanation for this are difficulties related to the In incorporation on non-polar planes. Indium incorporation is performed at relatively low temperatures, which can result in material with high defect densities.[22,23] For that reason, there has been a resurgence of interest in the growth of cubic, zincblende GaN (zb-GaN),[24–29] which when grown with a (001) orientation, is free from the internal electric fields. This eliminates the QCSE, ensures better overlap of the electron–hole wave function, and this leads to potentially higher radiative recombination efficiency. Additionally, it also has a narrower bandgap than wz-GaN, meaning less InN fraction is required in the active region to achieve the same green emission when compared with their wz-GaN-based devices.[30] However, because zb-GaN is metastable relative to wz-GaN, direct growth of zb-GaN material is prone to switching to the wurtzite phase during growth.[31] There are different approaches to achieve zb-GaN growth. One is the use of cubic substrates, such as 3C-SiC/Si, which has the advantage of being able to grow continuous epilayers.[32,33] However, the growth is challenging due to the metastability of zb-GaN, leading to stacking faults and inclusions of wz-GaN. Another approach, for the material used in this paper, is the growth on patterned substrates, where initially wz-GaN is grown on different exposed Si {111} facets in the Si substrate; once two wz-GaN [0001] growth fronts meet, a transition to zb-GaN occurs.[25,34–36] More details can be found in Sec. II.

Determining the integrity of the structure and identifying the presence of defects, misorientation and strain in zb-GaN materials is integral to understanding the growth and to improving material quality and device performance. Diffraction techniques, such as x-ray diffraction (XRD) and transmission electron microscopy (TEM), are routinely employed in the characterization of GaN semiconductors.[37] The scanning electron microscopy (SEM) technique of electron backscatter diffraction (EBSD) can also provide structural information.[25] It complements TEM in that it can provide similar information on defects, but may be used to analyze and image as-grown epitaxial samples with no sample preparation across areas ranging from tens of nanometers to several centimeters, albeit with lower spatial resolution. XRD provides valuable information on misorientation and strain but is generally not an imaging technique. EBSD can image misorientation and strain, albeit with lower sensitivity than XRD. In addition, recent advancements in EBSD analysis methods have led to the routine analysis of (mis)orientation, crystal polarity, strain, and defects in III-nitride semiconductors.[38–40]

In this paper, we utilize EBSD to investigate the crystallographic relationships between wz- and zb-GaN lattices grown upon micro-patterned Si (001) substrates, vastly expanding on the EBSD results in Ref. 25. As depicted in Figs. 1(a) and 1(b), the growth of zb-GaN is induced from wz-GaN growth fronts due to the patterning of the Si substrate and the subsequent growth of GaN on opposing Si {111} facets. Orientation measurements of the left and right wz-GaN regions, the central zb-GaN region, and the Si substrate allowed the determination of the epitaxial relationships and their misalignment. EBSD revealed that the orientation of the two wz-GaN [0001] growth directions is slightly misaligned. This misalignment is sufficient to induce misorientation within the zb-GaN such that the zb-GaN crystal lattice is bowed toward the structural interfaces between the hexagonal and cubic polytypes.

II. MATERIALS AND METHODS

Sample fabrication is a two-step process, distinguished by the patterning of a Si (100) substrate and the subsequent growth of GaN via metal organic vapor-phase epitaxy (MOVPE).[25,41,42] First, large area interference lithography was implemented to pattern a series of parallel stripes, with lengths parallel to the Si [110] direction. Subsequently, an anisotropic wet etch of KOH was used to form V-shaped grooves (or V-grooves) composed of adjacent Si ($\bar{1}$11) and (1$\bar{1}$1) facets as shown in the cross section schematic in Fig. 1(a). Each V-groove is separated by a distance of $\approx 4\ \mu$m and has a depth of $\approx 0.7\ \mu$m and a surface width of $\approx 1\ \mu$m.[25] Once the substrate was patterned, a 10 nm AlN nucleation layer was grown
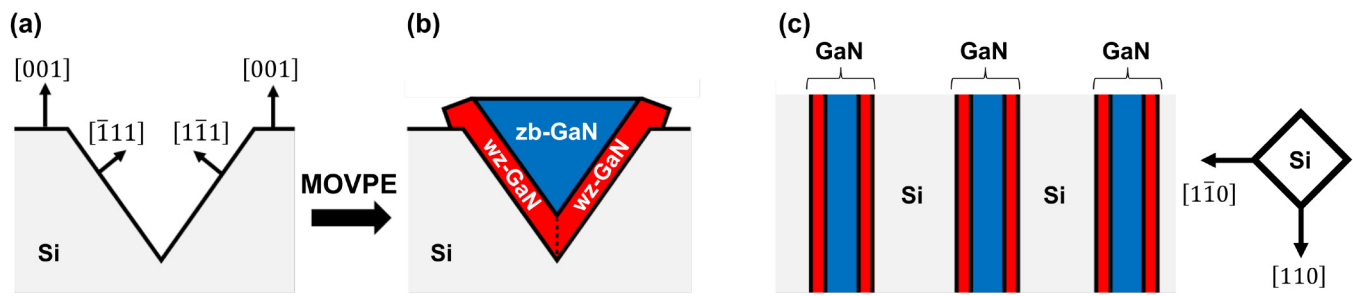
FIG. 1. Schematic depiction of the sample showing the expected growth of wz- and zb-GaN on patterned Si: (a) cross-sectional view of adjacent Si {111} facets that are exposed to form a V-shaped groove in the Si substrate. (b) Initial wz-GaN growth on the Si {111} facets results in converging wz-GaN {0001} interfaces, which coalesce and form a competing interface before undergoing a wurtzite-to-zincblende polytype transition to zb-GaN. The schematic, adopted from Ref. 41, is only an approximate illustration of the structure. (c) The periodic grooves are etched which results in the top surface to exhibit periodic stripes of GaN.

to prevent melt-back etching of Ga into the Si substrate,[43] followed by a 30 nm AlGaN buffer layer. GaN was then grown on the Si {111} facets to form a stripe of GaN on the sample top surface as shown in Fig. 1(c). GaN is expected to initially grow with a wurtzite structure and [0001] orientation perpendicular on the Si {111} facets,[44] thereby forming two converging wz-GaN growth fronts, as shown in Fig. 1(b), with different [0001] orientations. The two wz-GaN ⟨0001⟩ growth fronts are expected to coalesce with an angular difference of 109.5° which is required for zb-GaN to form due to the crystallographic relationship between the hexagonal and cubic lattices.[34,45]

The samples were characterized using the SEM-based technique of EBSD. EBSD is based on the diffraction of the electron beam by a crystal lattice and the subsequent detection of diffracted electrons that are backscattered from the sample surface. The diffracted electrons appear as an electron backscatter pattern (EBSP) composed of overlapping bands, where each band corresponds to a different crystallographic plane. By identifying the bands in an EBSP, it is possible to derive the structure, symmetry, and orientation of the sample under investigation. Figures 2(a) and 2(b) display example EPSPs from wz-GaN and zb-GaN, respectively, with several crystal planes highlighted. Planar EBSD measurements of the sample surface were performed using a variable pressure field emission gun SEM (FEI Quanta 250) and an Oxford Instruments Nordlys EBSD system. The cross-sectional EBSD measurements were performed using a field emission gun SEM (FEI Versa 3D) and an Oxford Instruments Symmetry S2 EBSD detector. All EBSD data were acquired with a surface tilt of 70° and an electron beam acceleration voltage of 20 kV. For the planar EBSD measurements, the EBSP size was $672 \times 512 \, px^2$ and a step size of 25 nm was used, whereas for the cross section, it was $622 \times 512 \, px^2$ and 20 nm. After initial indexing using the Oxford Instruments' Hough-based Refined Accuracy method, indexing was further refined using the pattern matching approach.[46] Here, the determination of crystal orientation was further optimized by finding the highest cross correlation coefficient between the experimental and dynamically simulated EBSP using the initial indexing as starting values.[47,48] The orientation precision in EBSD is typically of order 0.03° for pattern matched data and the orientation precision of the cross-sectional measurement was
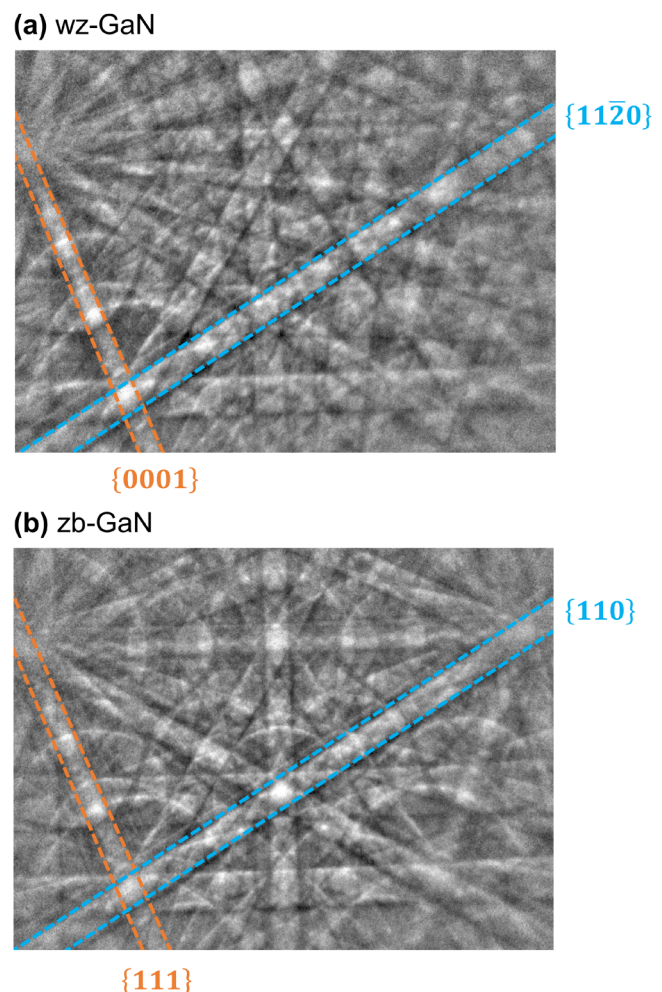

FIG. 2. Electron backscatter diffraction patterns (EBSPs) of the (a) wz-GaN and (b) zb-GaN crystal structures.

$\approx 0.018°$ as determined by the 95th percentile of the histogram of the kernel average misorientation (KAM) of the Si substrate.[46] Afterward, the EBSD data were analyzed using MTEX, a free EBSD toolbox for MATLAB, for the structure and orientation analysis.[49] For the cross-sectional measurement, a V-groove on the sample edge was polished using a focused ion beam (FIB, FEI Versa 3D). First, the top surface of the edge was covered with a W layer deposited with a 5 keV electron beam interacting with metal carrier gas. Subsequently, a larger layer of material on the edge was removed using the "cleaning cross-sectional method" and a 30 keV Ga ion beam. Final polishing of the cross section was performed using a 8 keV Ga ion beam; this enabled the recording of EBSPs with sufficient quality.

In EBSD, crystal orientations are described relative to chosen reference directions, the so-called sample or specimen reference frame. This describes the relation of the detector with respect to the sample and the orientation of the crystal lattice.[50] With respect to Fig. 1(c), we define the in-plane directions that are perpendicular and parallel to the fabricated V-grooves and the sample surface normal as the sample reference frame axes, denoted as the X-, Y-, and Z-axes, respectively.

III. RESULTS AND DISCUSSION

Figure 3(a) shows a secondary electron (SE) image of the sample surface with the area marked where EBSD was performed. The stripe in the center of the image is a GaN epitaxial layer which has grown inside of the Si V-groove. It is bordered by dark regions corresponding to the SiO$_2$ mask on top of the Si (001) substrate surface. Figure 3(b) shows a structure map for the surface distribution of wz- and zb-GaN polytypes. The distribution of wz- and zb-GaN regions relates well to theory, depicted schematically in Fig. 1, showing that wz-GaN initially develops, forming an interface with the Si substrate, before coalescing and undergoing a hexagonal-to-cubic polytype transition, leading to zb-GaN in the center of the stripe.

To understand the orientation relationship between the wz- and zb-GaN regions, inverse pole figure (IPF) maps were constructed from the EBSD data set. Figures 3(c)–3(e) show IPF maps in the X, Y, and Z sample frame directions, which correspond to the directions perpendicular and parallel to the V-groove (in-plane directions) and the sample normal direction (out-of-plane direction) as previously stated. The IPF maps plot the crystallographic directions using the crystallographic color keys shown in Figs. 3(f) and 3(g). From the IPF maps, we can see that the zb-GaN region has the same crystallographic orientation as the Si substrate such that both crystal structures are [001] oriented in Z and the $\langle 110 \rangle$ directions are parallel to the X and Y directions. Additionally, the left and right wz-GaN regions are oriented (and colored) similarly in X, Y, and Z reference directions, which suggests that they share an equivalent crystallographic relationship with respect to the Si substrate and zb-GaN region. From the IPF maps, we deduce that the $\langle 11\bar{2}0 \rangle$ direction of both wz-GaN regions are parallel to the length of the V-groove (Y direction) such that wz- and zb-GaN regions have a crystallographic relationship where $\langle 11\bar{2}0 \rangle_{wz} \parallel \langle 110 \rangle_{zb}$.[42]

Pole figure scatterplots were used to determine the crystallographic directions of the wz- and zb-GaN regions perpendicular and parallel to the stripe directions (X and Y directions) and the sample normal (Z direction) and determine the crystallographic relationship between the wz- and zb-GaN regions. Figures 4(a)–4(c) show the combined pole figures for crystal directions of the wz- and zb-GaN regions closest to the orientation of the X, Y, and Z sample reference axes. Markers, i.e., poles, in a pole figure correspond to a projection of a family of crystal directions, hence overlapping poles correspond to a shared direction between crystal lattices. Crystal directions parallel to the surface normal (Z) are plotted in the center of the pole figure, while in-plane directions (X and Y) are plotted at the edges of the pole figure. In each plot, there are different distributions observed for the left and right wz-GaN regions (enlarged in the inset panels), meaning their crystal lattices have slightly different orientations. However, they have poles which overlap (appearing as red ∗ symbols) in X, Y, and Z directions. This is consistent with the IPF maps for wz-GaN in Figs. 3(c)–3(e). The wz-GaN poles also overlap with zb-GaN poles in the X, Y, and Z directions with the following alignments: $\perp\{30\bar{3}8\}_{wz} \parallel \langle 110 \rangle_{zb}$, $\langle 11\bar{2}0 \rangle_{wz} \parallel \langle 110 \rangle_{zb}$, and $\perp\{30\bar{3}4\}_{wz} \parallel \langle 001 \rangle_{zb}$. The X and Y alignments of $\perp\{30\bar{3}8\}_{wz}$ and $\perp\{30\bar{3}4\}_{wz}$, respectively, are the lowest index orientations found and were informed by Ref. 35. This allows differences in orientation between the left and right wz-GaN regions to be investigated, as described later on. A schematic depiction of the unit cell orientation for the wz- and zb-GaN regions is presented in Fig. 5(b) which was derived from this crystallographic relationship.

Closer inspection of the in-plane poles (on the edge of the pole figure) perpendicular to the GaN stripe (X direction) and the sample normal direction (Z direction), depicted in Figs. 4(a) and 4(c), revealed a difference of $\approx 1.76°$ and $\approx 1.21°$ between the "overlapping" poles for left and right wz-GaN regions, respectively. The distribution of zb-GaN poles parallel to the X direction is located between left and right wz-GaN distributions, suggesting that the zb-GaN adopts an orientation which is the average of the two wz-GaN growth fronts. Comparatively, Fig. 4(b) depicts better alignment ($\approx 0.26°$) between the $\langle 11\bar{2}0 \rangle_{wz}$ and $\langle 110 \rangle_{zb}$ poles parallel to the Y direction. One explanation for the difference in orientation between the wz-GaN poles depicted in Figs. 4(a) and 4(c) is that the differences may derive from the c/a ratio of the wz-GaN crystal lattice. The orientations of the $\{30\bar{3}8\}$ and $\{30\bar{3}4\}$ semi-polar planes, unlike the orientation of the $\{11\bar{2}0\}$ polar planes, are dependent on the dimensions of both the c and a lattice parameters, i.e., they are not orthogonal to either the c or a direction. Consequently, while $\{30\bar{3}8\}$ and $\{30\bar{3}4\}$ are perpendicular for the ideal c/a ratio of 1.633, they are not exactly perpendicular even for unstrained GaN which has a c/a ratio of around 1.626.[52] Another explanation is that there is misalignment between the wz-GaN growth fronts about the Y direction, a feature which could develop depending on the precision of the etching process that formed the V-groove or from thermal and lattice mismatch between the wz-GaN growth fronts and the Si {111} sidewalls.

The pole figures in Fig. 5(a) show the distributions of poles for the $\langle 0001 \rangle_{wz}$ growth direction of the wz-GaN regions and the $\langle 111 \rangle_{zb}$ direction of the zb-GaN region. The [0001]$_{wz}$ orientation is
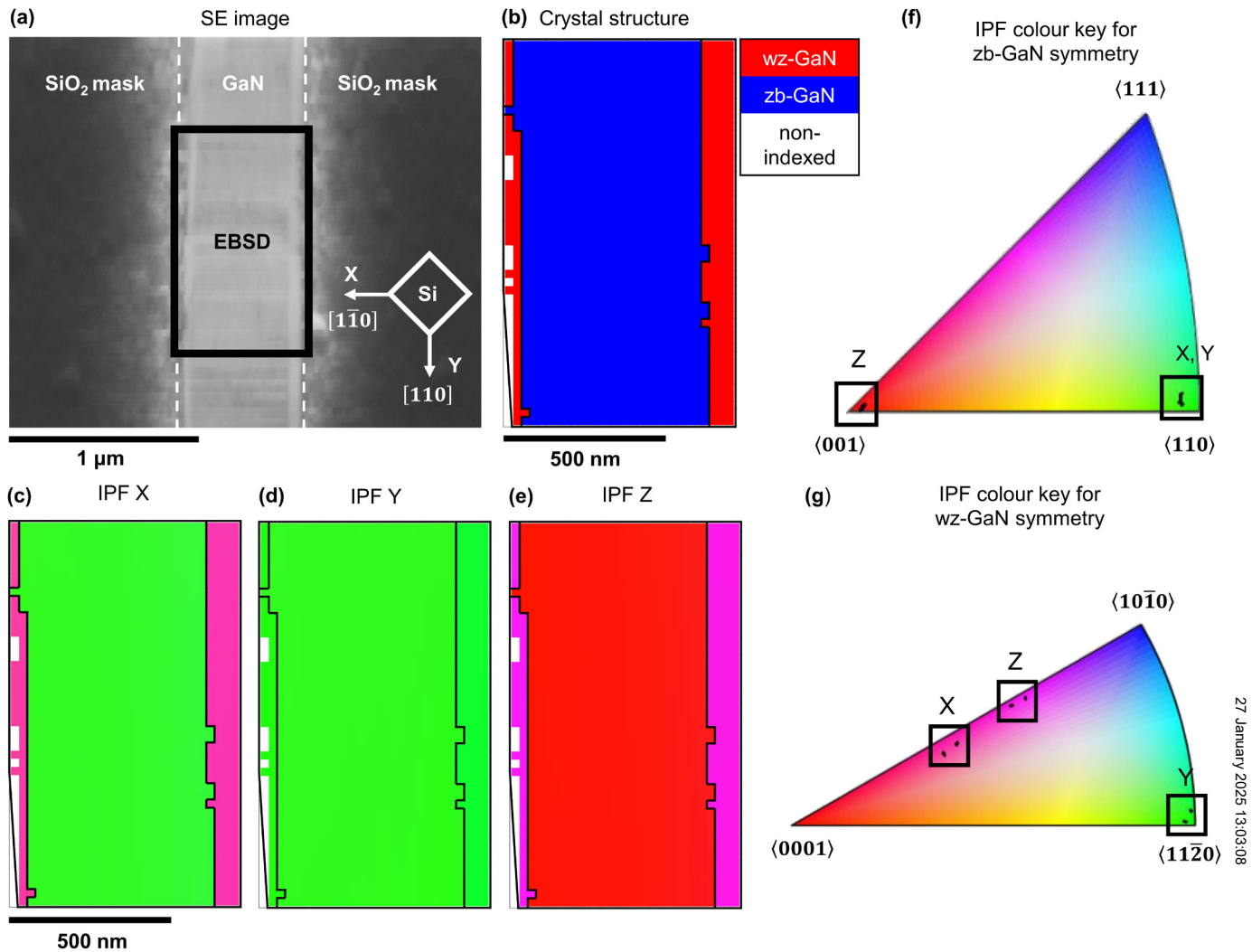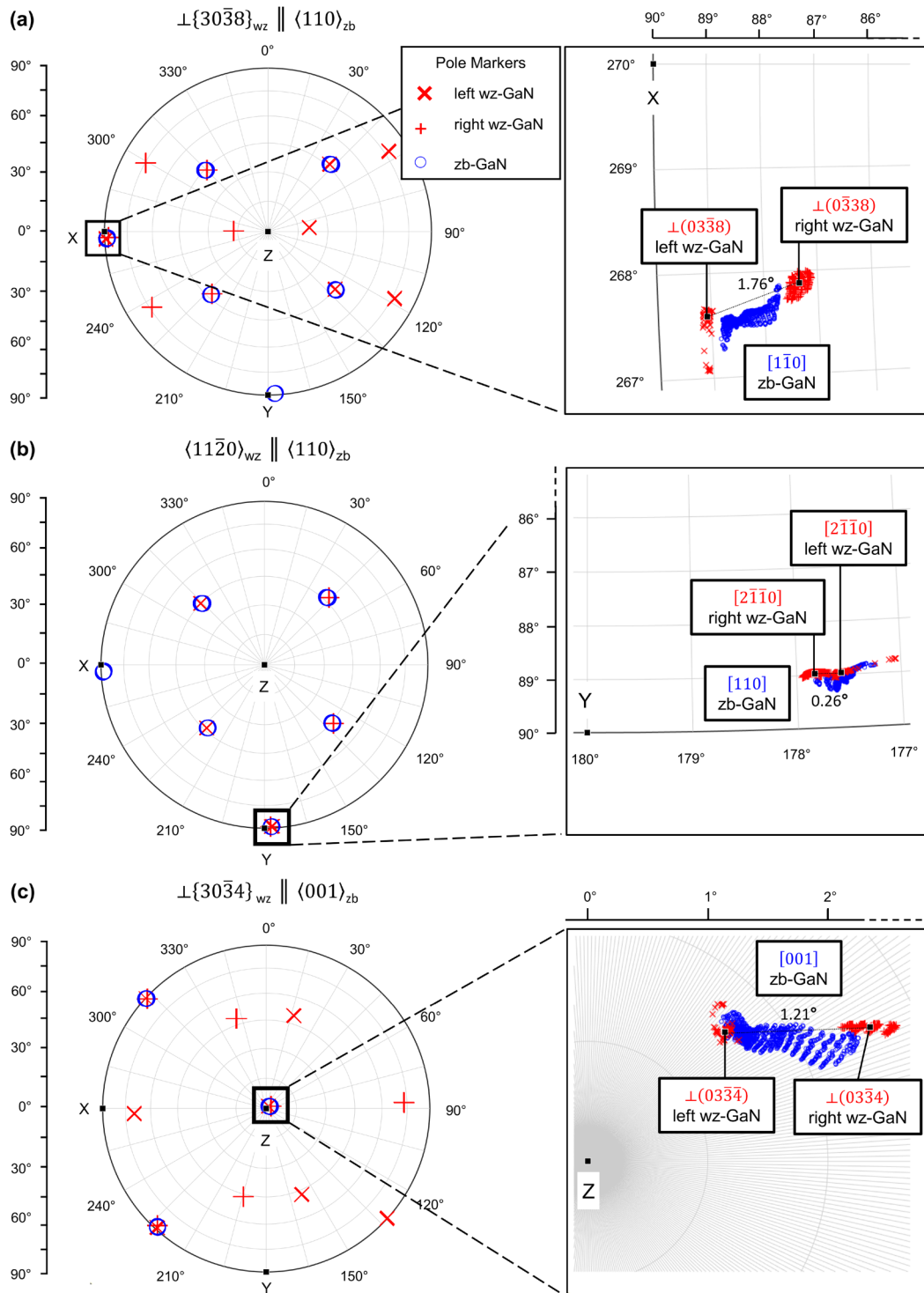
27 January 2025 13:03:08

FIG. 3. EBSD data set measured over a V-groove showing the distribution of the crystal structure and orientation after GaN deposition. (a) SE image of the sample surface showing a single stripe of GaN and the area over which EBSD was performed. (b) Crystal structure map constructed from the EBSD data set showing the occurrence of structural distribution of wz- and zb-GaN inside the V-groove. (c)–(e) Orientation maps or IPF maps showing the wz- and zb-GaN crystallographic directions perpendicular and parallel to the V-groove (X and Y directions) and the sample surface normal (Z direction). Crystallographic color key for the (f) zb-GaN and (g) wz-GaN crystal lattices are derived from the crystal symmetry.[51] Non-indexed regions (white) relate to areas with low cross correlation coefficient, excluded from the analysis. Boundaries between wz- and zb-GaN regions are marked using black lines.

independent of the c/a ratio, as it is perpendicular to the c-plane. In addition, $[111]_{zb}$ and $[0001]_{wz}$ are the close-packed directions of their respective crystal lattices, where their atomic arrangement differs only in terms of stacking sequence. Therefore, assuming that the wz-GaN growth fronts are properly aligned with the Si {111} facets, the $\langle 0001 \rangle_{wz}$ and $\langle 111 \rangle_{zb}$ poles should coincide similarly to the poles depicted in Fig. 4(b). Figure 5(a) shows two $\langle 0001 \rangle_{wz}$ distributions, corresponding to left and right wz-GaN regions, which align with different $\langle 111 \rangle_{zb}$ directions of zb-GaN. However, upon closer inspection, there is a small misalignment between the overlap between the $\langle 0001 \rangle_{wz}$ and $\langle 111 \rangle_{zb}$ distributions, which

suggests that the $\langle 0001 \rangle_{wz}$ growth fronts do not align perfectly. Table I summarizes the angular difference measured between the average orientation of the "overlapping" poles presented in Figs. 4 and 5(a). This shows that the crystallographic directions of the left and right wz-GaN regions are approximately parallel in the Y direction with a difference of $\approx 0.26°$. The angle between the growth directions, i.e., $\langle 0001 \rangle$ directions, is $\approx 107.97°$, which corresponds to a misalignment of $\approx 1.53°$ with respect to their expected alignment of $109.50°$.

To further investigate the epitaxial relationship between the zb-GaN and wz-GaN regions with the Si substrate, EBSD

FIG. 4. Composite pole figures scatterplots for wz- and zb-GaN regions, showing the crystallographic directions (poles) parallel to the (a) X, (b) Y, and (c) Z sample reference frame directions. The upper hemisphere of each pole figure is plotted with a grid resolution of 15°, while close-ups of crystallographic relationships in each inset are shown with a higher grid resolution of 1°. Table I provides a summary for the differences in orientation between left and right wz-GaN poles.
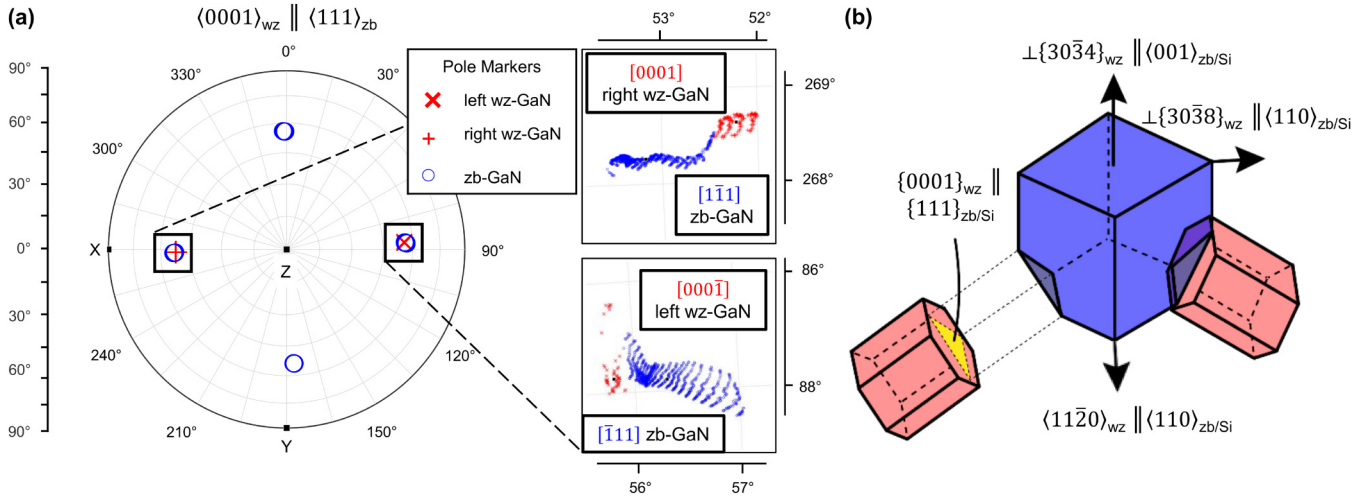
FIG. 5. (a) A composite pole figure scatterplot for close-packed $\langle 0001 \rangle_{wz}$ and $\langle 111 \rangle_{zb}$ directions of the wz- and zb-GaN lattices. The upper hemisphere of the pole figure is plotted with a grid resolution of $15°$, while close-ups of crystallographic relationships are plotted with a higher grid resolution of $1°$. (b) Schematic illustration of the crystallographic arrangement of wz- and zb-GaN regions. The Si substrate and the zb-GaN have the sample epitaxial relationship.

measurements were performed on a cross section across a V-groove that is shown in Fig. 6(a). This allowed simultaneous measurement of both GaN regions and Si. For the calculation of any misorientation or angular difference between directions, average orientations were calculated for the different regions and different poles in the pole figures (i.e., left and right wz-GaN, zb-GaN, and Si substrates) shown in Fig. 6(b). It should be noted that the misorientation analysis of the zb-GaN region presented later in Fig. 7 revealed that there is a misorientation of about $1°$ present across the zb-GaN region which is averaged over in this analysis. The angle between the left and right $\langle 0001 \rangle_{wz-GaN}$ growth fronts was determined to be $\approx 109.13°$, which corresponds to a misalignment of $\approx 0.37°$. This misalignment is much smaller compared with the planar measurement and is, for example, possibly due to measuring a different V-groove where the growth was better. Next, the alignment of the wz-GaN grown on the Si sidewalls and subsequently induced zb-GaN are investigated by calculating the angle between the $\langle 111 \rangle_{Si}$, $\langle 0001 \rangle_{wz-GaN}$, and $\langle 111 \rangle_{zb-GaN}$ directions for the interfaces

on the left and right sidewalls of the V-groove. The results are summarized in Table II. It is noteworthy that the wz-GaN shows a larger misalignment of the order of $0.2° - 0.3°$ to the material on either side along its growth direction. Whereas, comparing the $\langle 111 \rangle$ directions of the Si and the zb-GaN, with the wz-GaN sandwiched in-between, the misalignment is much smaller, on the order of $0.1°$.

Localized misorientation within the zb-GaN region was evaluated in Fig. 7 to determine whether or not the misalignment between the wz-GaN growth fronts would induce strain in zb-GaN. Misorientation was assessed by considering the difference (or deviation) in the orientation of each data point in the EBSD map with respect to a reference orientation, which is referred to as grain reference orientation deviation (GROD) analysis. Here, we have chosen the mean orientation of the zb-GaN region as the reference orientation. The magnitude of misorientation (GROD angle) and the axis around which this misorientation occurs (GROD axis) are shown in Figs. 7(a) and 7(b) with the color key for the GROD axis map shown in the pole figures in Fig. 7(c). To better visualize the direction of rotation relative to the sample features, Figs. 7(d)–7(f) show the magnitude of the rotation vector (or GROD axis) components relative to the X, Y, and Z sample reference frame axes and their histograms. The GROD angle, shown in Fig. 7(a), is used to visualize and understand the variation of misorientation of the zb-GaN microstructure. The misorientation angle is greatest (darker red) at the interface between the wz- and zb-GaN regions, while vertically adjacent data points exhibit relatively similar degrees (colors) of misorientation. This indicates that lattice misorientation derives from the interface between wurtzite and zincblende lattices. The GROD axis, which indicates the direction of the rotation, are mapped in Fig. 7(b) with respect to a direction-to-color key shown in Fig. 7(c). In the GROD axis map, we observe a distinct color change from left to right about angles of

TABLE I. Summary of the pole figure results from Figs. 4 and 5, showing the angular differences for normals of crystallographic planes for the left and right wz-GaN lattices. Measured alignments were calculated with respect to the mean orientation of the left and right wz-GaN poles.

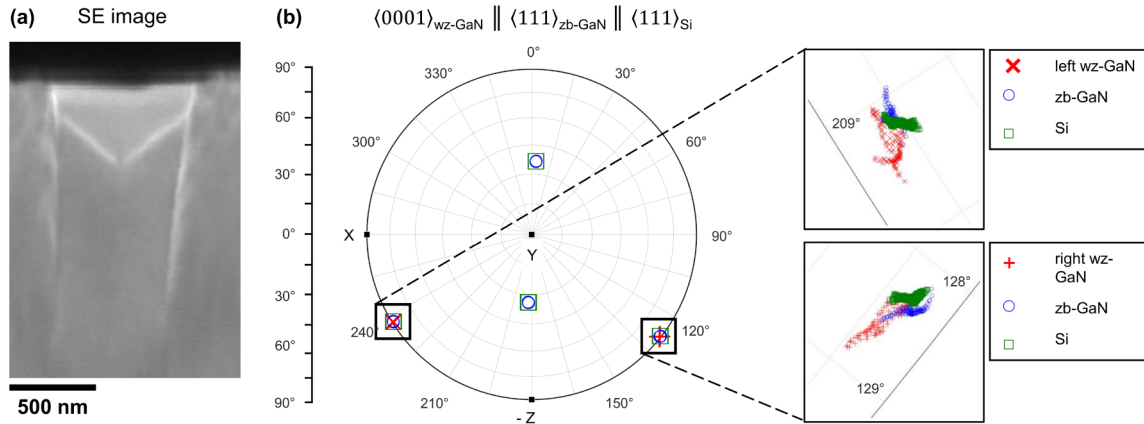| Left wz-GaN	Right wz-GaN	Difference (°)	Note
[000$\bar{1}$]	[0001]	107.97	Growth directions
⊥ (03$\bar{3}$8)	⊥ (0$\bar{3}$38)	1.76	Perpendicular to grooves
[2$\bar{1}\bar{1}$0]	[2$\bar{1}\bar{1}$0]	0.26	Parallel to grooves
⊥ (03$\bar{3}\bar{4}$)	⊥ (0$\bar{3}\bar{3}$4)	1.21	Sample normal

FIG. 6. (a) Cross-sectional SE image of the V-shaped groove measured by EBSD. (b) A composite pole figure scatterplot for close-packed $\langle 0001 \rangle_{wz-GaN}$, $\langle 111 \rangle_{zb-GaN}$, and $\langle 111 \rangle_{Si}$ directions of the wz- and zb-GaN lattices and the Si substrate from the cross-sectional EBSD measurement. The right hand side shows the overlapping poles associated with the GaN growth from the left and right {111} sidewalls of the Si groove. Considering that the EBSD measurement was performed on the polished cross section, the measurement geometry changed with respect to the crystallographic directions, hence the $\langle 0001 \rangle_{wz-GaN}$ and $\langle 111 \rangle_{zb-GaN}$ appear at different locations in the pole figure compared with the same pole figure from EBSD measurements of the top surface in Fig. 5. In order to keep consistent in notation, the labeling of the sample reference frame directions X (perpendicular to the V-groove), Y (parallel to the V-groove), and Z (parallel to the sample normal) is the same.
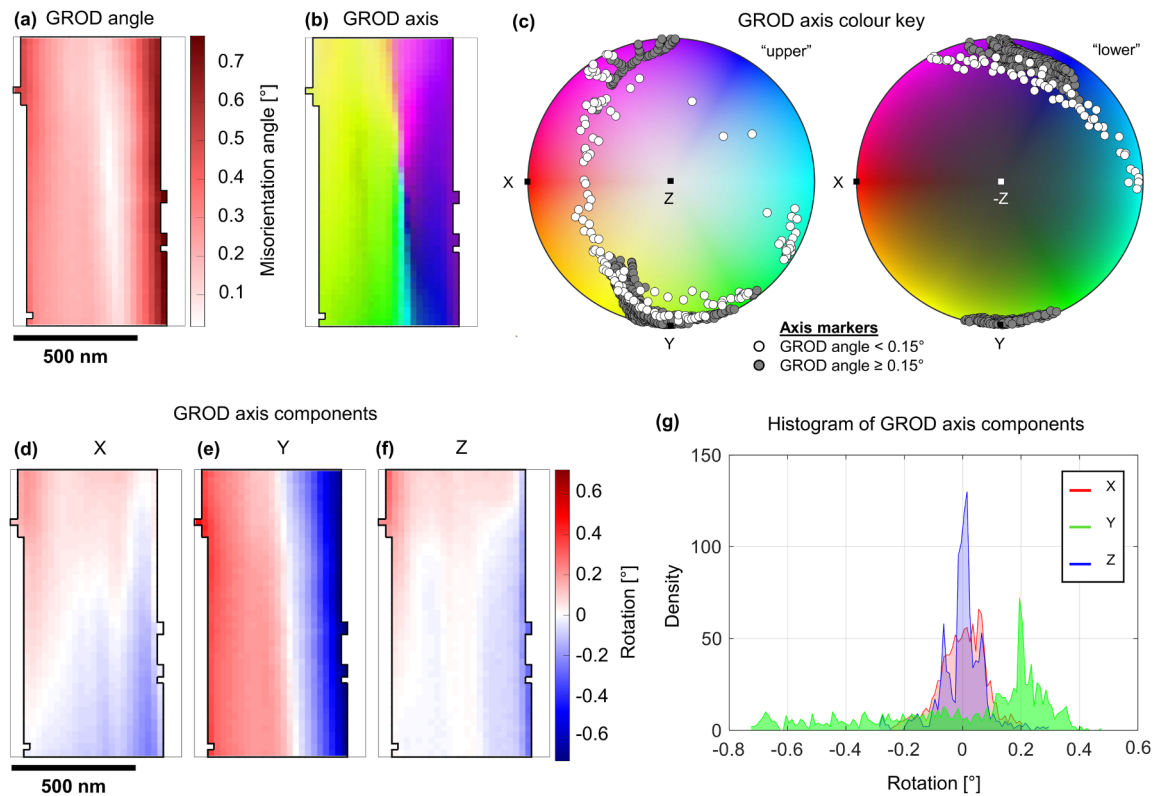

FIG. 7. Analysis of the misorientation within the zb-GaN region from Fig. 3. GROD maps for misorientation (a) angle and (b) axis showing the difference (deviation) in orientation between each data point with respect to the mean orientation of the zb-GaN. (c) The GROD axis color key is a pole figure showing the distribution of the rotation axes as poles plotted on stereographic projections of the upper and lower hemispheres of the sample reference frame. GROD axis component (d)–(f) maps and (g) histograms parallel to the X, Y, and Z sample reference frame directions.

27 January 2025 13:03:08

TABLE II. Summary of the pole figure results from Fig. 6, showing the angular differences between normal of the Si sidewall (Si ⟨111⟩), wz-GaN growth direction (⟨0001⟩), and induced zb-GaN materials (zb-GaN ⟨111⟩). Measured alignments were calculated with respect to the mean orientation of the left and right wz-GaN poles, the zb-GaN poles, and the Si poles.

Interfaces	Left side (°)	Right side (°)
Si ⟨111⟩ to wz-GaN ⟨0001⟩	0.24	0.28
wz-GaN ⟨0001⟩ to zb-GaN ⟨111⟩	0.27	0.30
Si ⟨111⟩ to zb-GaN ⟨111⟩	0.07	0.12

misorientation $\geq 0.15°$ [plotted as gray markers in Fig. 7(c)]. The color change corresponds to positive (green) and negative (purple) rotations about the Y sample direction (parallel to the V-groove). The GROD axis with angles of misorientation $< 0.15°$ [plotted as white markers in Fig. 7(c)] mark the transition from rotations about the Y and −Y direction in roughly the middle of the zb-GaN region—the reliability of which will be discussed later. The distribution of the GROD axis with angles $< 0.15°$ were interpreted by mapping the X, Y, and Z components of the GROD axis, as shown in Figs. 7(d)–7(f). The Y component, which has the largest
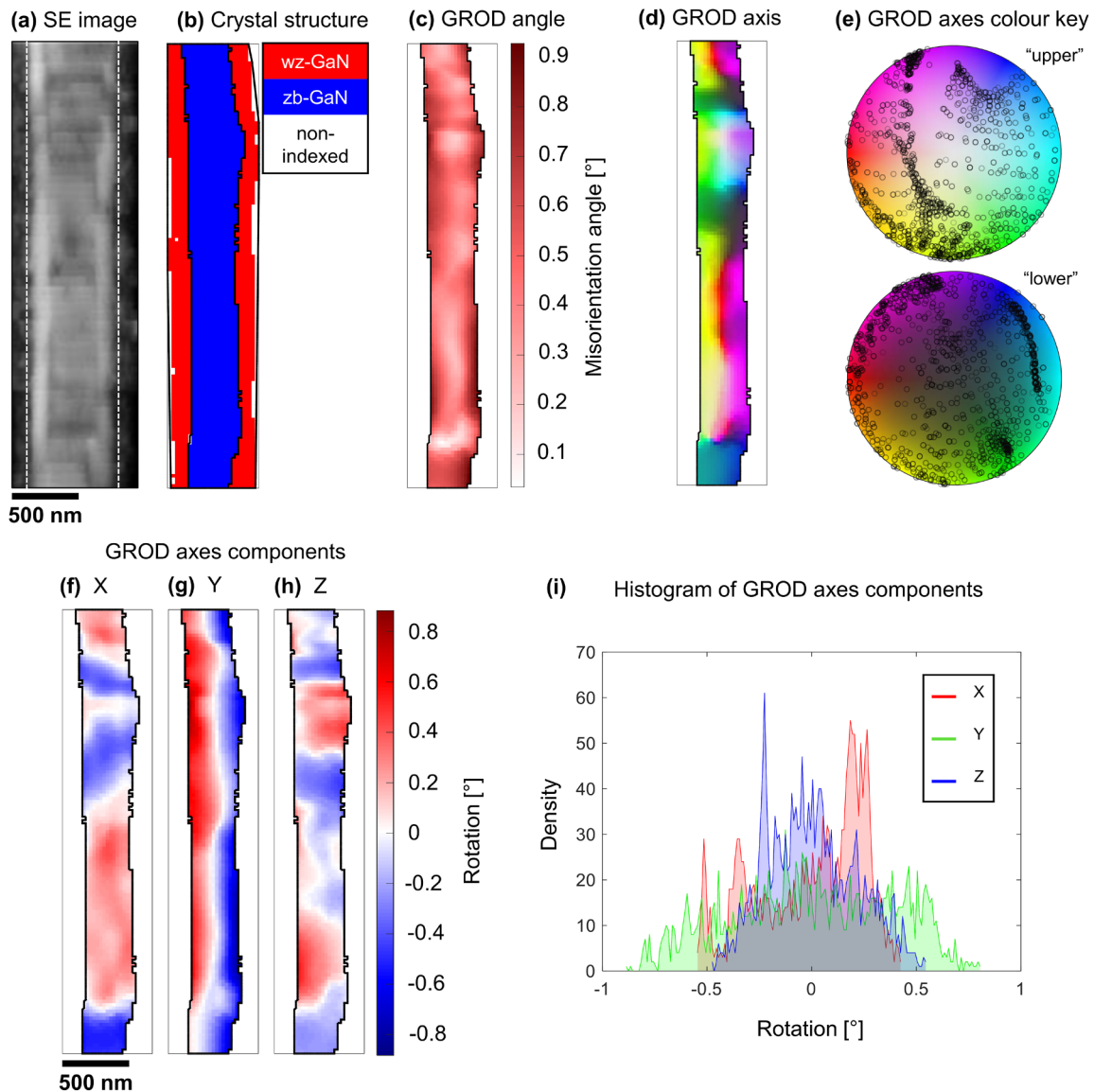

FIG. 8. GROD analysis from different V-groove measured over a larger acquisition area outlined in the (a) SE image using a white, dotted line. (b) Crystal structure map showing the distribution of the wz- and zb-GaN lattices inside of the V-groove. GROD (a) angle and (d) axis map with (e) color key. (f)–(h) GROD axis component maps parallel to the X, Y, and Z sample reference frame directions and their (i) histograms.

27 January 2025 13:03:08

magnitude of up to about $0.7°$, exhibits a transition from positive (red) to negative (blue) rotations with GROD angles $< 0.15°$, which correlates well with the color change from green to purple observed in Fig. 7(b) close to the middle of the zb-GaN region. The X and Z components are both similar in magnitude (up to about $0.3°$), are much smaller compared with the overall Y component, and have a color distribution which is distinctly different from the Y components. Generally, for small total GROD angles $< 0.15°$, we observed that the X and Z components have magnitudes either comparable to or exceeding the Y component. Therefore, regions with misorientation angles $< 0.15°$ have more dominant X and Z components relative to Y compared with regions with misorientation angles $\geq 0.15°$. Histograms of the GROD axis components, Fig. 7(g), show that the Y component has the broadest distribution of misorientation while X and Z components have peaks close to $0°$. A physical interpretation of the GROD analysis is that the zb-GaN crystal lattice is distorted and bends toward the wz-GaN interfaces about the length of the V-groove. This is consistent with the aforementioned misalignment between the wz-GaN growth fronts, which form a $\{0001\}_{wz} \parallel \{111\}_{zb}$ interface with the zb-GaN, and is strong evidence to suggest that misorientation in zb-GaN derives directly from its interfaces with the wz-GaN regions. These observations are consistent with XRD analysis from Ref. 42 where it was shown that the zb-GaN cubic unit cell was asymmetrically strained parallel and perpendicular to the V-groove. XRD showed that the zb-GaN lattice parameters increased due to tensile strain in the (001) plane, whereas the EBSD analysis expands on this observation and shows that the zb-GaN crystal lattice bends toward structural interfaces.

Subsequent EBSD measurements were performed on a larger area to confirm these observations; the SE image and crystal structure map are shown in Figs. 8(a) and 8(b), respectively. The GROD analysis of the zb-GaN region is shown in Figs. 8(c)–8(i). Again, the reference orientation is the mean orientation of all data points within the zb-GaN region. The GROD angle, displayed in Fig. 8(c), exhibits the same degree of misorientation as previously measured for the area in Fig. 7(a). The GROD axis, shown in Figs. 8(d) and 8(e), is more difficult to interpret and exhibits no preferred axis of rotation relative to the reference orientation. Additional factors are contributing to the misorientation within the sample than what is observed previously in Fig. 7. The GROD Y component still exhibits the broadest degree of rotation as shown in the GROD Y map and histogram in Figs. 8(g) and 8(i), respectively. However, the GROD X and Z components [Figs. 7(f) and 7(h)] are more dominant than previously observed. With respect to the maps of the GROD axis components, Figs. 8(f)–8(h), we observe that the Y component exhibits a single transition from positive to negative rotations, which occurs in the center of the zb-GaN region with low angles of misorientation (colors close to white). Meanwhile, transitions from positive to negative rotations about X and Z occur predominantly perpendicular to the stripe. The Y component [Fig. 8(g)] exhibits the same behavior as previously discussed, which is evidence to suggest that the zb-GaN is strained by the interface it forms with the wz-GaN regions, and that this is a feature that is consistent across multiple EBSD measurements of the sample. However, the origins of observation for the X and Z components are ambiguous. One possible explanation is that the X

and Z components relate to the initial growth mechanisms of zb-GaN as described in Ref. 41. TEM investigations showed that voids form sporadically along the bottom of the V-groove before converging to form the zb-GaN region. These voids lead to a discontinuity of zb-GaN at the bottom of the V-groove. Slight differences in orientation between these nucleation sites of the zb-GaN may lead to the observations in the GROD X and Z component maps in Figs. 8(f) and 8(h).

IV. CONCLUSIONS

The characterization of zb-GaN grown on a micro-pattered Si (001) substrate was performed using the SEM-based technique of EBSD. Initially, wz-GaN growth fronts form on the Si $\{111\}$ facets before undergoing a polytype transition to zb-GaN. Orientation analysis, using IPF maps and pole figures, revealed the following crystallographic relationship between the zb- and wz-GaN regions: $\perp\{30\bar{3}8\}_{wz} \parallel \langle 110 \rangle_{zb}$ perpendicular to the V-groove; $\langle 11\bar{2}0 \rangle_{wz} \parallel \langle 110 \rangle_{zb}$ parallel to the V-groove; and $\perp\{30\bar{3}4\}_{wz} \parallel \langle 001 \rangle_{zb}$ parallel to the sample normal. Furthermore, the wz-GaN growth fronts were found to share a $\{0001\}_{wz-GaN} \parallel \{111\}_{zb-GaN} \parallel \{111\}_{Si}$ crystallographic relationship with both the Si and zb-GaN growth fronts. The wz-GaN growth fronts were expected to coalesce with a $109.5°$ angle between the $\langle 0001 \rangle$ growth directions; however, they were misaligned by about $0.4° - 1.5°$ depending on which stripe was measured. From a cross-sectional measurement, the evolution of misalignment of the $\langle 0001 \rangle_{wz-GaN}$ growth direction with respect to the direction of the Si $\{111\}$ sidewall and the $\langle 111 \rangle_{zb-GaN}$ direction was determined to be in the range of $0.1° - 0.3°$. The misorientation (GROD) analysis revealed that the misalignment of the $\langle 0001 \rangle$ directions induces misorientation in the zb-GaN crystal lattice of similar magnitude to the misalignment between the growth fronts. Furthermore, it identified that the zb-GaN lattice is distorted and bends toward the wz-GaN interfaces about the direction parallel to the V-groove. Therefore, while the misorientation angles are $< 1°$ with respect to the reference orientation, the zb-GaN lattice is under strain due to misalignment of the wz-GaN growth fronts. The misorientation analysis over larger areas suggests that additional factors induce changes in the orientation of the zb-GaN lattice, which might relate to the initial growth conditions of zb-GaN.

AUTHOR DECLARATIONS
Conflict of Interest

The authors have no conflicts to disclose.

Author Contributions

Dale M. Waters: Conceptualization (supporting); Data curation (equal); Formal analysis (lead); Investigation (equal); Methodology (equal); Writing – original draft (lead); Writing – review & editing (supporting). **Bethany Thompson:** Formal analysis (supporting). **Gergely Ferenczi:** Formal analysis (supporting); Writing – review & editing (supporting). **Ben Hourahine:** Formal analysis (supporting); Funding acquisition (supporting); Writing – review & editing (supporting). **Grzegorz Cios:** Funding acquisition (supporting); Methodology (equal); Writing – review & editing (supporting). **Aimo Winkelmann:** Funding acquisition (supporting); Methodology (supporting); Writing – review & editing (supporting). **Christoph J. M. Stark:** Methodology (supporting); Resources (supporting); Writing – review & editing (supporting). **Christian Wetzel:** Funding acquisition (supporting); Methodology (supporting); Resources (supporting); Writing – review & editing (supporting). **Carol Trager-Cowan:** Conceptualization (supporting); Formal analysis (supporting); Funding acquisition (supporting); Investigation (supporting); Supervision (equal); Writing – review & editing (supporting). **Jochen Bruckbauer:** Conceptualization (lead); Data curation (equal); Formal analysis (supporting); Funding acquisition (supporting); Investigation (supporting); Supervision (equal); Writing – review & editing (lead).

DATA AVAILABILITY

The data associated with this research are available at https://doi.org/10.15129/1f65afc8-bc9d-4537-b016-76d55319eddb or from the corresponding author.

REFERENCES

[1]United Nations Environment Programme, "Accelerating the global adoption of energy-efficient lighting" (2017); available at https://www.unep.org/resources/publication/accelerating-global-adoption-energy-efficient-lighting.

[2]J. Y. Tsao, M. E. Coltrin, M. H. Crawford, and J. A. Simmons, "Solid-state lighting: An integrated human factors, technology, and economic perspective," Proc. IEEE **98**, 1162 (2010).

[3]M. Usman, M. Munsif, U. Mushtaq, A.-R. Anwar, and N. Muhammad, "Green gap in GaN-based light-emitting diodes: In perspective," Crit. Rev. Solid State Mater. Sci. **46**, 450 (2021).

[4]M. H. Crawford, "LEDs for solid-state lighting: Performance challenges and recent advances," IEEE J. Sel. Top. Quantum Electron. **15**, 1028 (2009).

[5]Q. Lv, J. Liu, C. Mo, J. Zhang, X. Wu, Q. Wu, and F. Jiang, "Realization of highly efficient InGaN green LEDs with sandwich-like multiple quantum well structure: Role of enhanced interwell carrier transport," ACS Photonics **6**, 130 (2018).

[6]A. I. Alhassan, N. G. Young, R. M. Farrell, C. Pynn, F. Wu, A. Y. Alyamani, S. Nakamura, S. P. DenBaars, and J. S. Speck, "Development of high performance green c-plane III-nitride light-emitting diodes," Opt. Express **26**, 5591 (2018).

[7]J. Piprek, "Energy efficiency analysis of GaN-based blue light emitters," ECS J. Solid State Sci. Technol. **9**, 015008 (2019).

[8]C. Wetzel, T. Salagaj, T. Detchprohm, P. Li, and J. S. Nelson, "GaInN/GaN growth optimization for high-power green light-emitting diodes," Appl. Phys. Lett. **85**, 866 (2004).

[9]M. A. der Maur, A. Pecchia, G. Penazzi, W. Rodrigues, and A. Di Carlo, "Efficiency drop in green InGaN/GaN light emitting diodes: The role of random alloy fluctuations," Phys. Rev. Lett. **116**, 027401 (2016).

[10]Y. Li, S. You, M. Zhu, L. Zhao, W. Hou, T. Detchprohm, Y. Taniguchi, N. Tamura, S. Tanaka, and C. Wetzel, "Defect-reduced green GaInN/GaN light-emitting diode on nanopatterned sapphire," Appl. Phys. Lett. **98**, 151102 (2011).

[11]F. Bernardini, V. Fiorentini, and D. Vanderbilt, "Spontaneous polarization and piezoelectric constants of III-V nitrides," Phys. Rev. B **56**, R10024 (1997).

[12]T. Takeuchi, S. Sota, M. Katsuragawa, M. Komori, H. Takeuchi, H. A. H. Amano, and I. A. I. Akasaki, "Quantum-confined Stark effect due to piezoelectric fields in GaInN strained quantum wells," Jpn. J. Appl. Phys. **36**, L382 (1997).

[13]S.-p. Wan, J.-b. Xia, and K. Chang, "Effects of piezoelectricity and spontaneous polarization on electronic and optical properties of wurtzite III–V nitride quantum wells," J. Appl. Phys. **90**, 6210 (2001).

[14]T. Detchprohm, M. Zhu, Y. Li, Y. Xia, C. Wetzel, E. A. Preble, L. Liu, T. Paskova, and D. Hanser, "Green light emitting diodes on a-plane GaN bulk substrates," Appl. Phys. Lett. **92**, 241109 (2008).

[15]K. Akita, T. Kyono, Y. Yoshizumi, H. Kitabayashi, and K. Katayama, "Improvements of external quantum efficiency of InGaN-based blue light-emitting diodes at high current density using GaN substrates," J. Appl. Phys. **101**, 033104 (2007).

[16]F. Nippert, S. Y. Karpov, G. Callsen, B. Galler, T. Kure, C. Nenstiel, M. R. Wagner, M. Straßburg, H.-J. Lugauer, and A. Hoffmann, "Temperature-dependent recombination coefficients in InGaN light-emitting diodes: Hole localization, Auger processes, and the green gap," Appl. Phys. Lett. **109**, 161103 (2016).

[17]T. Takeuchi, H. Amano, and I. Akasaki, "Theoretical study of orientation dependence of piezoelectric effects in wurtzite strained GaInN/GaN heterostructures and quantum wells," Jpn. J. Appl. Phys. **39**, 413 (2000).

[18]P. Waltereit, O. Brandt, A. Trampert, H. Grahn, J. Menniger, M. Ramsteiner, M. Reiche, and K. Ploog, "Nitride semiconductors free of electrostatic fields for efficient white light-emitting diodes," Nature **406**, 865 (2000).

[19]H. Ng, "Molecular-beam epitaxy of GaN/Al$_x$Ga$_{1-x}$N multiple quantum wells on R-plane (10$\bar{1}$2) sapphire substrates," Appl. Phys. Lett. **80**, 4369 (2002).

[20]T. Koida, S. Chichibu, T. Sota, M. Craven, B. Haskell, J. Speck, S. DenBaars, and S. Nakamura, "Improved quantum efficiency in nonpolar (11$\bar{2}$0) AlGaN/GaN quantum wells grown on GaN prepared by lateral epitaxial overgrowth," Appl. Phys. Lett. **84**, 3768 (2004).

[21]P. Dawson, S. Schulz, R. Oliver, M. Kappers, and C. Humphreys, "The nature of carrier localisation in polar and nonpolar InGaN/GaN quantum wells," J. Appl. Phys. **119**, 181505 (2016).

[22]D. A. Browne, E. C. Young, J. R. Lang, C. A. Hurni, and J. S. Speck, "Indium and impurity incorporation in InGaN films on polar, nonpolar, and semipolar GaN orientations grown by ammonia molecular beam epitaxy," J. Vac. Sci. Technol. A **30**, 041513 (2012).

[23]A. Senichev, B. Dzuba, T. Nguyen, Y. Cao, M. A. Capano, M. J. Manfra, and O. Malis, "Impact of growth conditions and strain on indium incorporation in non-polar m-plane (10$\bar{1}$0) InGaN grown by plasma-assisted molecular beam epitaxy," APL Mater. **7**, 121109 (2019).

[24]M. R. Krames, O. B. Shchekin, R. Mueller-Mach, G. O. Mueller, L. Zhou, G. Harbers, and M. G. Craford, "Status and future of high-power light-emitting diodes for solid-state lighting," J. Disp. Technol. **3**, 160 (2007).

[25]C. J. Stark, T. Detchprohm, S. Lee, Y.-B. Jiang, S. Brueck, and C. Wetzel, "Green cubic GaInN/GaN light-emitting diode on microstructured silicon (100)," Appl. Phys. Lett. **103**, 232107 (2013).

[26]A. Gundimeda, M. Frentrup, S. M. Fairclough, M. J. Kappers, D. J. Wallis, and R. A. Oliver, "Investigation of wurtzite formation in MOVPE-grown zincblende GaN epilayers on Al$_x$Ga$_{1-x}$N nucleation layers," J. Appl. Phys. **131**, 115703 (2022).

[27]J. Lee, Y. C. Chiu, M. A. Johar, and C. Bayram, "Structural and optical properties of cubic GaN on U-grooved Si (100)," Appl. Phys. Lett. **121**, 032101 (2022).

[28]D. J. Binks, P. Dawson, R. A. Oliver, and D. J. Wallis, "Cubic GaN and InGaN/GaN quantum wells," Appl. Phys. Rev. **9**, 041309 (2022).

[29]M. F. Zscherp, S. A. Jentsch, M. J. Müller, V. Lider, C. Becker, L. Chen, M. Littmann, F. Meier, A. Beyer, D. M. Hofmann, D. J. As, P. J. Klar, K. Volz,

S. Chatterjee, and J. Schörmann, "Overcoming the miscibility gap of GaN/InN in MBE growth of cubic In$_x$Ga$_{1-x}$N," ACS Appl. Mater. Interfaces **15**, 39513 (2023).

[30] I. Vurgaftman, J. á. Meyer, and L. á. Ram-Mohan, "Band parameters for III–V compound semiconductors and their alloys," J. Appl. Phys. **89**, 5815 (2001).

[31] N. Zainal, S. Novikov, A. Akimov, C. Staddon, C. Foxon, and A. Kent, "Hexagonal (wurtzite) GaN inclusions as a defect in cubic (zinc-blende) GaN," Physica B **407**, 2964 (2012).

[32] D. J. As, T. Frey, D. Schikora, K. Lischka, V. Cimalla, J. Pezoldt, R. Goldhahn, S. Kaiser, and W. Gebhardt, "Cubic GaN epilayers grown by molecular beam epitaxy on thin β-SiC/Si (001) substrates," Appl. Phys. Lett. **76**, 1686 (2000).

[33] T. Wade, A. Gundimeda, M. Kappers, M. Frentrup, S. Fairclough, D. Wallis, and R. Oliver, "MOVPE studies of zincblende GaN on 3C-SiC/Si(001)," J. Cryst. Growth **611**, 127182 (2023).

[34] S. C. Lee, X. Y. Sun, S. D. Hersee, S. R. J. Brueck, and H. Xu, "Spatial phase separation of GaN selectively grown on a nanoscale faceted Si surface," Appl. Phys. Lett. **84**, 2079 (2004).

[35] S. C. Lee, B. Pattada, S. D. Hersee, Y.-B. Jiang, and S. R. J. Brueck, "Nanoscale spatial phase modulation of GaN on a V-grooved Si substrate-cubic phase GaN on Si(001) for monolithic integration," IEEE J. Quantum Electron. **41**, 596 (2005).

[36] C. Bayram, J. A. Ott, K.-T. Shiu, C.-W. Cheng, Y. Zhu, J. Kim, M. Razeghi, and D. K. Sadana, "Cubic phase GaN on nano-grooved Si (100) via maskless selective area epitaxy," Adv. Funct. Mater. **24**, 4492 (2014).

[37] M. Frentrup, L. Y. Lee, S.-L. Sahonta, M. J. Kappers, F. Massabuau, P. Gupta, R. A. Oliver, C. J. Humphreys, and D. J. Wallis, "X-ray diffraction analysis of cubic zincblende III-nitrides," J. Phys. D: Appl. Phys. **50**, 433002 (2017).

[38] G. Naresh-Kumar, J. Bruckbauer, A. Winkelmann, X. Yu, B. Hourahine, P. Edwards, T. Wang, C. Trager-Cowan, and R. Martin, "Determining GaN nanowire polarity and its influence on light emission in the scanning electron microscope," Nano Lett. **19**, 3863 (2019).

[39] C. Trager-Cowan, A. Alasmari, W. Avis, J. Bruckbauer, P. R. Edwards, G. Ferenczi, B. Hourahine, A. Kotzai, S. Kraeusel, G. Kusch, R. W. Martin, R. McDermott, G. Naresh-Kumar, M. Nouf-Allehiani, E. Pascal, D. Thomson, S. Vespucci, M. D. Smith, P. J. Parbrook, J. Enslin, F. Mehnke, C. Kuhn, T. Wernicke, M. Kneissl, S. Hagedorn, A. Knauer, S. Walde, M. Weyers, P.-M. Coulon, P. A. Shields, J. Bai, Y. Gong, L. Jiu, Y. Zhang, R. M. Smith, T. Wang, and A. Winkelmann, "Structural and luminescence imaging and characterisation of semiconductors in the scanning electron microscope," Semicond. Sci. Technol. **35**, 054001 (2020).

[40] K. P. Hiller, A. Winkelmann, B. Hourahine, B. Starosta, A. Alasmari, P. Feng, T. Wang, P. J. Parbrook, V. Z. Zubialevich, S. Hagedorn, S. Walde, M. Weyers, P.-M. Coulon, P. A. Shields, J. Bruckbauer, and C. Trager-Cowan, "Imaging threading dislocations and surface steps in nitride thin films using electron backscatter diffraction," Microsc. Microanal. **29**, 1879 (2023).

[41] S. Lee, Y. Jiang, M. Durniak, C. Wetzel, and S. Brueck, "Initial stage of cubic GaN for heterophase epitaxial growth induced on nanoscale v-grooved Si (001) in metal-organic vapor-phase epitaxy," Nanotechnology **30**, 025711 (2018).

[42] M. T. Durniak, A. S. Bross, D. Elsaesser, A. Chaudhuri, M. L. Smith, A. A. Allerman, S. C. Lee, S. R. Brueck, and C. Wetzel, "Green emitting cubic GaInN/GaN quantum well stripes on micropatterned Si (001) and their strain analysis," Adv. Electron. Mater. **2**, 1500327 (2016).

[43] H. Ishikawa, G.-Y. Zhao, N. Nakada, T. Egawa, T. Jimbo, and M. Umeno, "GaN on Si substrate with AlGaN/AlN intermediate layer," Jpn. J. Appl. Phys. **38**, L492 (1999).

[44] D. Zhu, D. J. Wallis, and C. J. Humphreys, "Prospects of III-nitride optoelectronics grown on Si," Rep. Prog. Phys. **76**, 106501 (2013).

[45] T. Araki, T. Minami, and Y. Nanishi, "Microstructures of cubic and hexagonal GaN grown on (0001) sapphire by ECR-MBE with various electric biases," Phys. Status Solidi A **176**, 487 (1999).

[46] A. Winkelmann, B. M. Jablon, V. Tong, C. Trager-Cowan, and K. Mingard, "Improving EBSD precision by orientation refinement with full pattern matching," J. Microsc. **277**, 79 (2020).

[47] A. Winkelmann, C. Trager-Cowan, F. Sweeney, A. P. Day, and P. Parbrook, "Many-beam dynamical simulation of electron backscatter diffraction patterns," Ultramicroscopy **107**, 414 (2007).

[48] G. Nolze, M. Jürgens, J. Olbricht, and A. Winkelmann, "Improving the precision of orientation measurements from technical materials via EBSD pattern matching," Acta Mater. **159**, 408 (2018).

[49] F. Bachmann, R. Hielscher, and H. Schaeben, "Texture analysis with MTEX-free and open source software toolbox," in *Solid State Phenomena* (Trans Tech Publications Ltd., 2010), Vol. 160, p. 63.

[50] T. Britton, J. Jiang, Y. Guo, A. Vilalta-Clemente, D. Wallis, L. Hansen, A. Winkelmann, and A. Wilkinson, "Tutorial: Crystal orientations and EBSD—Or which way is up?" Mater. Charact. **117**, 113 (2016).

[51] G. Nolze and R. Hielscher, "Orientations—Perfectly colored," J. Appl. Crystallogr. **49**, 1786 (2016).

[52] M. A. Moram, Z. H. Barber, and C. J. Humphreys, "Accurate experimental determination of the Poisson's ratio of GaN using high-resolution x-ray diffraction," J. Appl. Phys. **102**, 023505 (2007).

27 January 2025 13:03:08